Optical response of the Dirac semimetals GdSb0.56Te1.35 and GdSb0.45Te1.50: influence of charge density wave distortion and magnetic order

Serto Rojewski, Raphael Borkenhagen, Runhan Li, Diego García Ovalle, Stepan S. Tsirkin, Harish Kumar, K. Raju, Raman Sankar, S. Lei, L. M. Schoop, Maia G. Vergniory, Christine A. Kuntscher

Angaben zur Veröffentlichung / Publication details:

Rojewski, Serto, Raphael Borkenhagen, Runhan Li, Diego García Ovalle, Stepan S. Tsirkin, Harish Kumar, K. Raju, et al. 2026. "Optical response of the Dirac semimetals GdSb0.56Te1.35 and GdSb0.45Te1.50: influence of charge density wave distortion and magnetic order." *Physical Review B* 113 (15): 155141. https://doi.org/10.1103/nygm-n4fv.

Optical response of the Dirac semimetals $GdSb_{0.56}Te_{1.35}$ and $GdSb_{0.45}Te_{1.50}$: Influence of charge density wave distortion and magnetic order

S. Rojewski,[1] R. Borkenhagen,[1] Runhan Li,[2] Diego García Ovalle,[2] Stepan S. Tsirkin,[3] Harish Kumar,[1] K. Raju,[4] Raman Sankar,[4] S. Lei,[5,6] L. M. Schoop,[5] Maia G. Vergniory,[2,7,8] and C. A. Kuntscher[1]

[1]*Experimentalphysik II, Institute for Physics, University of Augsburg, D-86135 Augsburg, Germany*

[2]*Département de Physique et Institut Quantique, Université de Sherbrooke, Sherbrooke, Québec, Canada J1K 2R1*

[3]*Chair of Computational Condensed Matter Physics, Institute of Physics, École Polytechnique Fédérale de Lausanne (EPFL), CH-1015 Lausanne, Switzerland*

[4]*Institute of Physics, Academia Sinica, Taipei 11529, Taiwan*

[5]*Department of Chemistry, Princeton University, Princeton, New Jersey 08544, USA*

[6]*Department of Physics, Hong Kong University of Science and Technology, Hong Kong, China*

[7]*Donostia International Physics Center, Paseo Manuel de Lardizabal 4, 20018 Donostia-San Sebastian, Spain*

[8]*Regroupement Québécois sur les Matériaux de Pointe (RQMP), Québec, Canada H3T 3J7*

(Received 15 July 2025; revised 10 March 2026; accepted 25 March 2026; published 20 April 2026)

The square-net materials $GdSb_xTe_{2-x-\delta}$ provide a platform for exploring the effects of charge density wave (CDW) distortion and band filling on the topological electronic band structure. In this work we use infrared spectroscopy to probe the temperature-dependent electronic excitations in $GdSb_{0.56}Te_{1.35}$ and $GdSb_{0.45}Te_{1.50}$ single crystals for different polarization directions parallel to the square-net layers. First-principles calculations were also performed to study the electronic band structure and interband optical conductivity of stoichiometric GdSbTe. For $GdSb_{0.56}Te_{1.35}$ the in-plane optical conductivity is independent of the polarization direction and contains a small Drude term, indicating a weak metallic character, and a pronounced near-infrared absorption band, which may be due to excitations across the CDW gap. Upon cooling, the optical response shows no significant temperature dependence within the experimental uncertainty, and no signatures associated with magnetic ordering are detected. In comparison, for $GdSb_{0.45}Te_{1.50}$ we observe an in-plane anisotropy and strongly reduced low-frequency optical conductivity, with small temperature dependence. Possible signatures of Dirac fermion excitations in the optical conductivity spectra are also analyzed and discussed. Our results demonstrate that small differences in the stoichiometry have a significant impact on the optical response of $GdSb_xTe_{2-x-\delta}$ materials.

DOI: 10.1103/nygm-n4fv

I. INTRODUCTION

The square-net materials MXZ (M = Zr, Hf, or lanthanides; X = Si, Ge, Sn, or Sb; Z = O, S, Se, or Te) provide a unique platform for exploring exotic physics induced by the interplay of nontrivial band topology, magnetism, Kondo effect, and charge-density-wave distortions [1]. Among them, nonmagnetic ZrSiS raised tremendous attention as a prototype nodal-line semimetal [2–7], whose characteristic features in the electronic band structure can be manipulated by the chemical pressure effect in ZrXZ compounds [8–10]. GdSbTe, another member of the MXZ material family, contains slabs of five square nets, with a stacking sequence (Te-Gd-Sb-Gd-Te) [see Fig. 1(a)] [8]. The Sb square net is sandwiched between two Gd square nets, where each Sb has bonding to four Gd atoms in tetrahedral coordination. The slabs are terminated by Te square nets on the two sides of the quintuple layer. As compared to ZrSiS, the presence of f electrons of the Gd atoms can lead to additional phenomena such as magnetic order and Kondo effect [1,11–13].

Indeed, GdSbTe has garnered significant attention recently due to its unique electronic and magnetic properties, such as a Dirac-like state robust against magnetic ordering with multiple Fermi surface pockets, making it an ideal platform to study the interplay of magnetism and topological states [14,15]. The band structure near E_F is characterized by linear band crossings, primarily originating from the Sb p_x and p_y orbitals. In the absence of SOC, these linear band crossing points (Dirac nodes) connect to form a diamond-shaped Fermi pocket around the Γ point of the Brillouin zone [16,17]. There is an additional Dirac nodal line (NL) along the X-U direction, whose nodal points at the high-symmetry X and U points are not gapped by SOC due to nonsymmorphic symmetry protection [16]. The low-temperature magnetic transition is driven by the alignment of localized magnetic moments of the $4f$ electrons, which can form one of four possible antiferromagnetic (AFM) spin configurations below $T_N \sim 12$ K. In Fig. 1(a) we illustrate one suggested spin configuration, i.e., an antiferromagnetically coupled ferromagnetic zigzag chain structure (AFM-A) [15]. Despite the similarities in crystal structure and electronic band structure with the nonmagnetic materials ZrSiS [6] and LaSbTe [18], Ref. [15] reports drastically different electrical transport properties of GdSbTe, namely an overall reduced dc

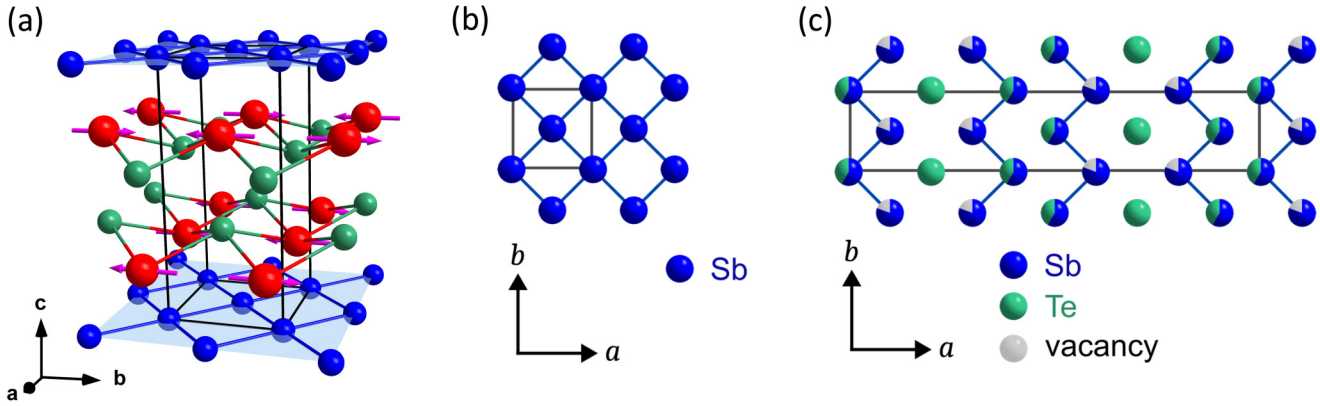

FIG. 1. (a) PbFCl-type crystal structure of GdSbTe with space group $P4/nmm$. The solid black line denotes the unit cell. The proposed AFM spin configuration below $T_N \sim 12$ K, depicted by pink arrows, illustrates the spins aligned along the *ab* plane according to Ref. [15]. (b) Square-net lattice of Sb atoms along the *ab* plane in tetragonal GdSbTe without structural distortions. The unit cell is given by the black square. (c) Corresponding square-net lattice of orthorhombic $GdSb_{0.45}Te_{1.50}$ (space group *Pmmn*) with CDW formation along the *a* direction, where the Sb sites are partially vacant or occupied by Te atoms according to Ref. [16]. The supercell is indicated by the black rectangle.

conductivity with a nonmetallic temperature dependence, likely influenced by 7/2 Gd-spin scattering [19]. The origin of the localization of charge carriers in GdSbTe is still under discussion.

Generally, the square-net configuration of atoms is conducive to crystal lattice distortions with the formation of charge density waves (CDWs), a collective electronic state characterized by periodic modulations of the charge density [20,21]. Due to the quasi-two-dimensional nature of square-net structures, the electrons are more confined in certain directions, which amplifies fluctuations that favor CDW formation [22,23]. The development of CDWs has been observed in the square-net rare-earth ditellurides $LnTe_2$ (Ln = lanthanide element) [1,24–30], and this phenomenon might contribute to the rich physical properties of GdSbTe as well [17,31,32]. CDW formation has been suggested for several *Ln*SbTe compounds including GdSbTe [17,31,33]. In particular, recent studies report a well-developed CDW already at room temperature in $GdSb_{0.46}Te_{1.48}$, with a high CDW transition temperature of $T_C \sim 950$ K [16]. Furthermore, it was shown that nonstoichiometric materials $GdSb_xTe_{2-x-\delta}$ with $x \leqslant 0.85$ (with δ indicating the vacancy level) exhibit CDWs that significantly alter their electronic and magnetic properties [16,34–36].

In $GdSb_xTe_{2-x-\delta}$ the Sb sites are partially vacant or occupied by Te atoms and a periodic lattice modulation arises concomitant with the emergence of CDWs, as illustrated in Fig. 1(c) for $GdSb_{0.45}Te_{1.5}$ [16]. X-ray diffraction (XRD) and transmission electron microscopy (TEM) measurements on various $GdSb_xTe_{2-x-\delta}$ solid solutions reveal the transition from a simple tetragonal square-net structure [see Fig. 1(b)] to more complex superstructures as the concentration of Sb changes. $GdSb_{0.85}Te_{1.15}$, which crystallizes in a tetragonal crystal symmetry, undergoes an antiferromagnetic phase transition. In contrast, compounds with lower Sb content and orthorhombic symmetry exhibit multiple magnetic transitions [35]. The evolution in crystal structure thus coincides with modifications in magnetic ordering, indicating an intricate interplay of crystal symmetry, CDW distortions, and magnetism [35].

The effect of CDW distortions on the electronic properties of $GdSb_xTe_{2-x-\delta}$ includes the opening of energy gaps in the electronic band structure, particularly around the Fermi level, while preserving the nonsymmorphically protected Dirac nodes. This preservation is significant because it suggests that the topological properties of the material are robust against the perturbations caused by the CDW as long as the nonsymmorphic symmetry is intact [34]. The Sb content x not only determines the lattice distortions but also the position of the Fermi level and hence the electronic band filling.

In order to further explore the effect of CDW distortions on the electronic properties in nonstoichiometric $GdSb_xTe_{2-x-\delta}$ compounds, we studied the optical response of two representatives, $GdSb_{0.56}Te_{1.35}$ and $GdSb_{0.45}Te_{1.50}$, and compared it to that of the nodal-line semimetals GdSbTe and ZrSiS reported in the literature. To this end, we carried out polarization-dependent and temperature-dependent reflectivity measurements on single crystals, for obtaining the optical conductivity over a broad frequency range. The experimental results are supplemented by first-principles calculations of the electronic band structure and interband optical conductivity of stoichiometric GdSbTe. Our results demonstrate the sensitivity of the optical properties of $GdSb_xTe_{2-x-\delta}$ materials regarding small differences in their stoichiometry. We also discuss possible signatures of Dirac fermion excitations in the measured optical conductivity spectra.

II. METHODS

$GdSb_{0.56}Te_{1.35}$ single crystals were grown by the chemical vapor transport method as reported in Ref. [15]. The samples had *ab* surface areas of 1 × 2 mm and were polished by using 0.1 μm diamond abrasive paper. The stoichiometry of the crystals was determined by energy-dispersive x-ray spectroscopy. DC magnetic susceptibility χ(T) measurements were performed in the temperature range of 2–300 K using a superconducting quantum interference device (SQUID) magnetometer (Quantum Design magnetic property measurement system, MPMS). $GdSb_{0.56}Te_{1.35}$ shows two magnetic phase transitions as depicted in Fig. 2: The transition at $T_N \sim 12$ K

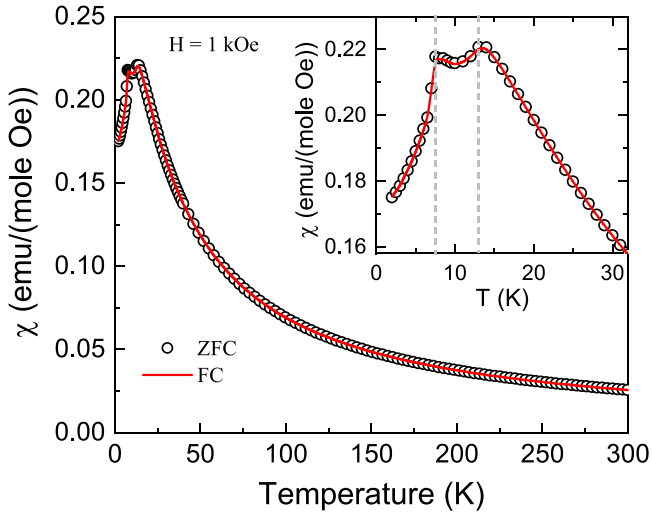

FIG. 2. Magnetic susceptibility of $GdSb_{0.56}Te_{1.35}$ as a function of temperature, showing an AFM phase transition at $T_N \sim 12$ K and spin reorientation transition at ~7.5 K.

corresponds to the AFM ordering of Gd spins, while the second transition at $T_{SR} \sim 7.5$ K is attributed to spin reorientation [15].

$GdSb_{0.45}Te_{1.50}$ single crystals were grown by chemical vapor transport and characterized by x-ray diffraction, energy-dispersive x-ray spectroscopy, magnetic susceptibility, transition electron microscopy, and electrical transport measurements as described in detail in Refs. [16,35].

Reflectivity measurements were conducted using an infrared microscope (Bruker Hyperion) with a 15× Cassegrain objective connected to a Bruker Vertex 80v FT-IR spectrometer in the frequency range 150–23 000 cm^{-1}. Polarizers were inserted into the beam path, in order to produce linearly polarized electromagnetic radiation for probing the anisotropic optical response within the *ab* plane, i.e., parallel to the square-net layer. The beam spot size amounted to ~80 μm in the midinfrared frequency range, whereas ~200 μm in the other measured ranges. At ambient temperature, a commercial Al mirror served as the reference. For reflectivity measurements at temperatures ranging from 300 to 4 K a CryoVac Konti cryostat was employed. The temperature difference between the cold finger and the sample remained small over the entire range, amounting to 0.4 K at room temperature, 0.3 K at 150 K, and 0.1 K at 4 K. Half of the surface of the freshly polished sample was coated with a layer of gold, serving as the reference for obtaining the absolute reflectivity. Positioned on a sample holder within the cryostat, the *ab* sample surface was aligned perpendicular to the incoming infrared beam. The data were measured for the far-infrared to visible frequency range (150–16 000 cm^{-1}).

All measured reflectivity spectra were extrapolated to low frequencies based on a Drude-Lorentz fit, while the high-frequency domains were extended using x-ray atomic scattering functions. Further, the optical functions were determined through the Kramers-Kronig (KK) relations, employing software programs developed by Tanner [37]. The optical spectra were then analyzed using the Drude-Lorentz model and the software REFFIT for fitting [38].

First-principles calculations were performed within the framework of density functional theory (DFT), employing the projector augmented wave (PAW) method as implemented in the Vienna *ab initio* simulation package (VASP) [39,40]. The exchange-correlation potential was described using the Perdew-Burke-Ernzerhof (PBE) formulation of the generalized gradient approximation (GGA) [41]. A plane-wave cutoff energy of 500 eV was used throughout the calculations. To account for the on-site Coulomb interaction, the GGA + U approach was adopted, with Hubbard U values of 4, 6, and 8 eV applied to the Gd-f electrons. To better reflect the symmetry of the experimental crystal structure, a slight distortion was introduced by allowing the a and b lattice constants to differ. A $2 \times 2 \times 1$ supercell was constructed to calculate the AFM-A/AFM-I magnetic configuration. The Brillouin zone was sampled using a uniform $8 \times 8 \times 4$ k-point mesh for the primitive cell and a $4 \times 4 \times 4$ mesh for the supercell. Maximally localized WANNIER functions (MLWFs) were constructed using the WANNIER90 code [42], based on the first-principles electronic structure obtained from VASP. The optical conductivity was calculated using the WANNIERBERRI code [43].

III. RESULTS AND DISCUSSION

A. Optical response of $GdSb_{0.56}Te_{1.35}$

The reflectivity spectrum of single-crystalline $GdSb_{0.56}Te_{1.35}$ is presented in Fig. 3(a) for the highest and lowest measured temperature. The optical response shows no polarization dependence within the *ab* plane. The moderately high reflectivity level at low frequencies and the presence of a broad plasma edge at ~500 cm^{-1} suggest the semimetallic nature of the material. Above 2000 cm^{-1} the reflectivity remains approximately constant up to ~6000 cm^{-1}, exhibiting a plateaulike behavior, followed by a steady decrease. It is important to note that a smooth, polished surface minimizes scattering and removes any surface contaminants or oxidation layers that might alter the optical response, as demonstrated by the comparison between the reflectivity spectra measured on an as-grown and a polished surface [see inset of Fig. 3(a)].

The corresponding optical conductivity spectra σ_1, as obtained from the measured reflectivity through KK analysis, are shown in Fig. 3(b). The metallic character of $GdSb_{0.56}Te_{1.35}$ is weak, as evidenced by the low value of the optical conductivity ($\sigma_1 < 700\ \Omega^{-1}cm^{-1}$) below ~500 cm^{-1} for all measured temperatures. For higher energies, we observe a pronounced near-infrared (NIR) absorption band located at ~6000 cm^{-1}, which has an almost linear-in-frequency behavior on its low-energy side. Above 12 000 cm^{-1} σ_1 is almost flat.

Upon cooling, the optical response remains largely temperature independent over the entire investigated energy range. Only very small variations are observed: the low-energy optical conductivity shows a marginal reduction, while a correspondingly weak increase is found in the NIR range, indicative of a minor redistribution of spectral weight, while the total spectral weight is conserved within the visible range, as shown in Fig. S11 in the Supplemental Material [45]. No systematic energy shift of the NIR absorption feature

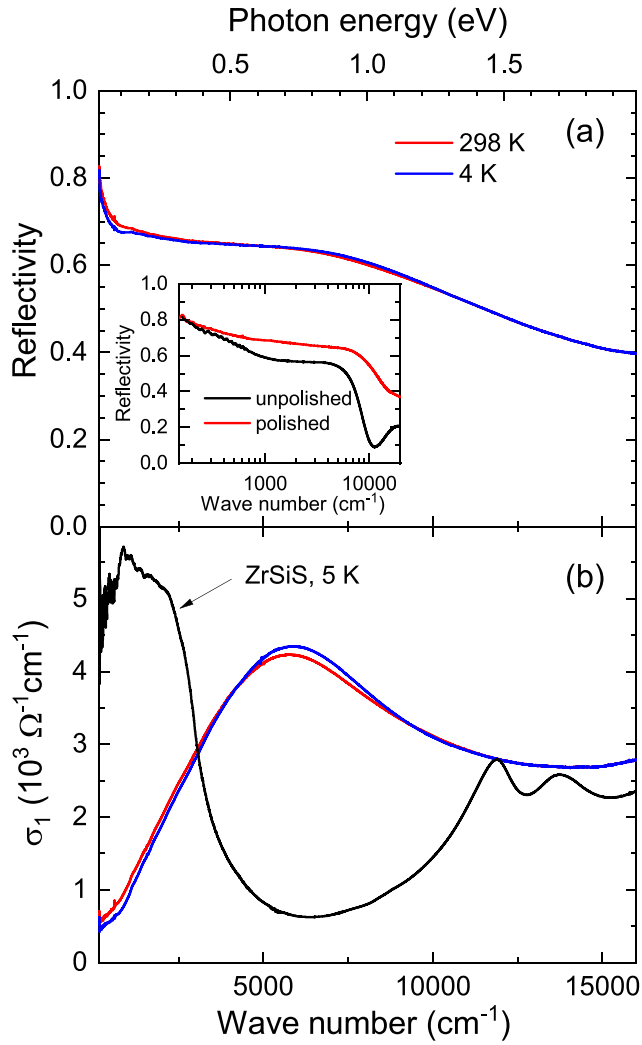

FIG. 3. (a) Reflectivity and (b) optical conductivity σ_1 spectra of $GdSb_{0.56}Te_{1.35}$ along the square-net layers (*ab* plane) for 298 and 4 K. For comparison, we include in (b) the optical conductivity spectrum of ZrSiS at 5 K from Ref. [44]. Inset in (a): Reflectivity spectra of $GdSb_{0.56}Te_{1.35}$ measured on as-grown and polished surfaces.

is detected. Moreover, no anomalies are observed at the magnetic phase transition, indicating the absence of a measurable coupling between magnetic and charge degrees of freedom.

For further analysis, we performed a quantitative analysis of our data by a simultaneous fit of both reflectivity and optical conductivity using the Drude-Lorentz model according to [46]

$$\sigma(\omega) = \frac{\omega_{\mathrm{pl}}^2}{4\pi(\Gamma_{\mathrm{D}} - i\omega)} + \sum_j \frac{\Psi_j^2}{4\pi} \frac{\omega}{i\left(\omega_{0,j}^2 - \omega^2\right) + \omega\Gamma_j}, \quad (1)$$

where the first term accounts for intraband transitions (Drude term), while the second term represents interband excitations (Lorentz oscillators). ω_{pl} and Γ_{D} are the plasma frequency and width of the Drude term, respectively, whereas Ψ_j, Γ_j, and $\omega_{0,j}$ are the oscillator strength, width, and resonant frequency of the j-th Lorentz oscillator, respectively. As an example, we show in Fig. 4 the fit of the σ_1 spectrum at 4 K to-

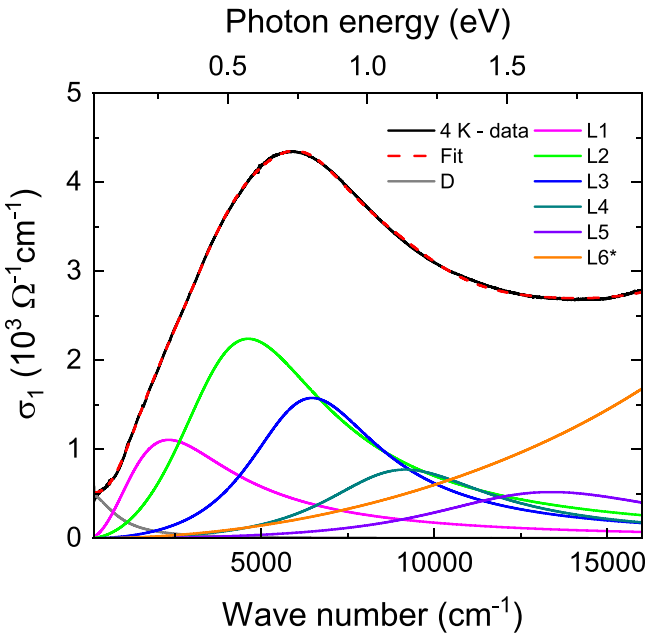

FIG. 4. Real part of the optical conductivity σ_1 of $GdSb_{0.56}Te_{1.35}$ at 4 K, together with the total Drude-Lorentz fit and the various fit contributions: one Drude (D) and six Lorentz (L) oscillators. The Lorentz term L6* denotes the sum of higher-energy excitations.

gether with the Drude and Lorentz contributions. The data can be reasonably well fitted by implementing one Drude and five Lorentz terms in the measured frequency range for all temperatures. Fits excluding the Drude contribution were also tested; however, they result in pronounced deviations in the low-energy FIR range (see Supplemental Material [45]). The pronounced NIR absorption band is mainly captured by the L2 and L3 Lorentz oscillator .

Upon cooling, the *dc* conductivity reduces from $\sim$600 Ω^{-1}cm^{-1} at 298 K to $\sim$500 Ω^{-1}cm^{-1} at 4 K, which is in agreement with resistivity measurements in Ref. [16]. The plasma frequency ω_{pl} of the Drude contribution, whose oscillator strength is proportional to ω_{pl}^2, decreases from the value 5795 cm^{-1} (0.72 eV) at 298 K to 5060 cm^{-1} (0.63 eV) at 4 K.

B. Optical response of $GdSb_{0.45}Te_{1.50}$

The polarization-dependent reflectivity spectra of $GdSb_{0.45}Te_{1.50}$ are presented in Fig. 5(a) for two selected temperatures (300 and 5 K). For comparison, we inserted the reflectivity spectrum of $GdSb_{0.56}Te_{1.35}$ at 5 K. Although the overall shape of the spectrum remains similar, the reflectivity of the $GdSb_{0.45}Te_{1.50}$ is lower over the entire studied spectral range compared to $GdSb_{0.56}Te_{1.35}$. In particular, in the far-infrared range the reflectivity level is at least 20% below that of $GdSb_{0.56}Te_{1.35}$. For $GdSb_{0.45}Te_{1.50}$ only slight variations in the reflectivity spectrum are observed during cooling.

The corresponding polarization-dependent optical conductivity spectra σ_1 are shown in Fig. 5(b). In comparison to $GdSb_{0.56}Te_{1.35}$ (ω_{pl}=0.63 eV at 4 K), the low-energy σ_1 of $GdSb_{0.45}Te_{1.50}$ is strongly reduced ($\omega_{\mathrm{pl}} \leqslant 0.19$ eV and $\omega_{\mathrm{pl}} \leqslant$

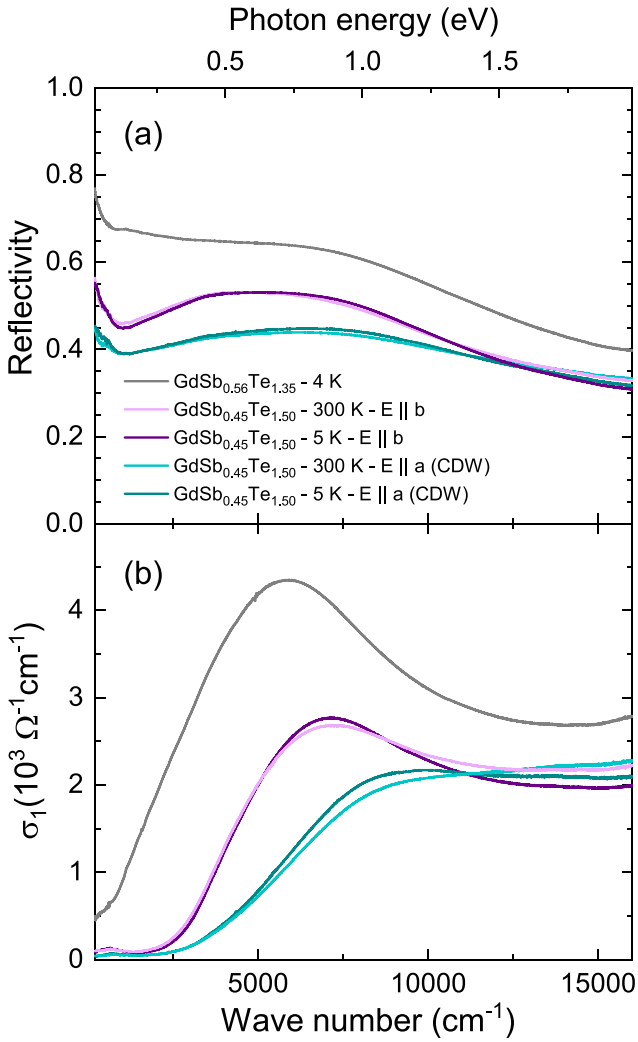

FIG. 5. (a) Reflectivity and (b) optical conductivity (σ_1) spectra of $GdSb_{0.45}Te_{1.50}$ for E$\|a$ (CDW direction) and E$\|b$ at 300 and 5 K, as compared to $GdSb_{0.56}Te_{1.35}$ at 4 K for the polarization E$\|ab$.

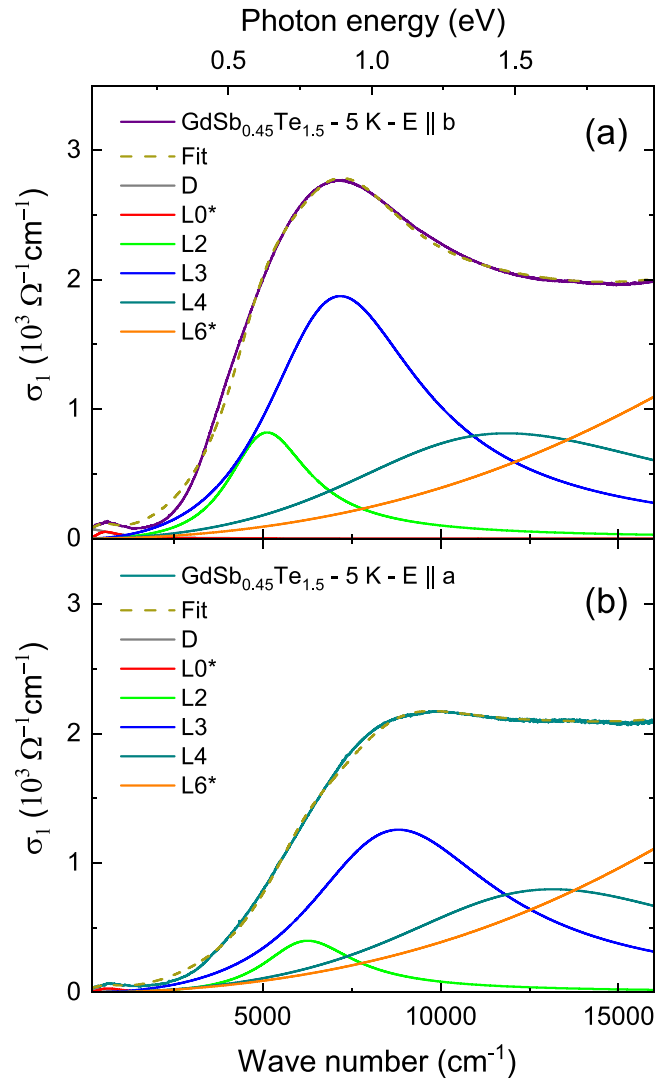

FIG. 6. Optical conductivity σ_1 of $GdSb_{0.45}Te_{1.50}$ for E$\|b$ and E$\|a$ (CDW direction) at 5 K, together with the total Drude-Lorentz fit and the individual fit contributions. The fitting model follows the approach used for $GdSb_{0.56}Te_{1.35}$, with the omission of L1 and L5 and the addition of an L0* oscillator in the far-infrared range.

0.28 eV for E$\|a$ and E$\|b$, respectively; please see the Supplemental Material for more information [45]). We assign the polarization direction with the stronger suppression of the low-energy optical conductivity to the E$\|a$ direction, along which the CDW is developed [see Fig. 1(c)]. Furthermore, the almost linear-in-frequency increase in the optical conductivity spectra for both compounds is followed by an NIR absorption band, which is located at 5400 cm^{-1} for $GdSb_{0.56}Te_{1.35}$ and 7200 cm^{-1} for $GdSb_{0.45}Te_{1.50}$ for E$\|b$. Along the CDW direction, E$\|a$, no clear NIR absorption band is present, but the linear-in-frequency increase is followed by an almost flat behavior. For both directions the σ_1 spectrum evidences nonmetallic behavior with an energy gap of the size 0.9–1.1 eV. The absence of itinerant carrier excitations in the optical response is in agreement with the nonmetallic temperature dependence of the *dc* resistivity, with an increase with decreasing temperature following a power law [16]. On the other hand, ARPES data in the same study show ungapped Dirac nodes protected by nonsymmorphic symmetry at several high symmetry points of the Brillouin zone and in close vicinity to E_F, which should cause low-frequency electronic excitations in the optical conductivity spectra, in contrast to our findings.

The optical response of $GdSb_{0.45}Te_{1.50}$ was analyzed using a similar Drude-Lorentz fitting model as for $GdSb_{0.56}Te_{1.35}$, but omitting L1 and L5 oscillators, which indicates the absence of corresponding interband excitations, respectively (see Fig. 6). An additional Lorentzian term, L0*, was introduced in the far-infrared range to capture the emerging small peak, which might be due to a damped phonon mode. Furthermore, all remaining oscillators within the measured frequency range exhibit a blueshift as compared to $GdSb_{0.56}Te_{1.35}$. It is interesting to note that the optical conductivity shows a flat behavior in the high-energy range for both polarization directions [see Fig. 5(b)]. Generally, a flat optical conductivity is suggestive for two-dimensional (2D) Dirac fermion excitations related to NL, as will be discussed in more detail below.

C. Signatures of CDW formation in $GdSb_{0.56}Te_{1.35}$ and $GdSb_{0.45}Te_{1.50}$

The profiles of the optical conductivity of $GdSb_{0.56}Te_{1.35}$ and $GdSb_{0.45}Te_{1.50}$ are markedly different from that of GdSbTe, which has a higher overall optical conductivity and higher σ_{dc} values ranging from ∼12 400 to ∼30 100 $\Omega^{-1}cm^{-1}$ at 300 and 10 K, respectively, as reported in Ref. [33]. Clearly, the excitations of itinerant charge carriers are much more pronounced in GdSbTe: Here, two Drude terms were implemented in the fit model, yielding a total plasma frequency of $\omega_{pl} \sim 21\,600\,cm^{-1}$ (2.68 eV) and $\sigma_{dc} \sim 30\,100\,\Omega^{-1}cm^{-1}$ at 10 K. The optical conductivity spectrum of GdSbTe also contains absorption peaks, which are located at a slightly lower frequency ∼3000 cm^{-1} at 10 K with a much more pronounced temperature dependence (blueshift during cooling). These midinfrared (MIR) absorption peaks have been interpreted in terms of excitations across CDW gaps [33].

The possible presence of CDWs in "stoichiometric" *Ln*SbTe compounds, including GdSbTe, was suggested in several earlier reports [17,33]. According to angle-resolved photoemission experiments on CeSbTe combined with density-functional-theory calculations [31], the Fermi surface of CeSbTe shows nesting, i.e., the Fermi surface contains parallel sheets, which can be connected by a wave vector. In the presence of strong electron-phonon coupling, this can lead to the development of a CDW accompanied by crystal lattice distortion [20]. As a consequence, an energy gap opens at the Fermi surface. Superstructure peaks in low-energy electron diffraction patterns confirm the presence of a CDW in CeSbTe in a wide temperature range (12–338 K) [31].

In general, the CDW formation is expected to have a big impact on the profile of the optical conductivity spectrum: The opening of a CDW gap reduces the free charge carrier density, causing a reduction or suppression of the Drude peak in the low-energy optical conductivity spectrum. This will also result in the transfer of spectral weight from the Drude peak to higher frequencies, typically in the MIR and NIR ranges, indicative of the energy required to break the CDW state and excite electrons across the CDW gap [21,47–50]. As the temperature decreases, the CDW gap widens, causing the MIR/NIR peaks to shift to higher frequencies, reflecting the increasing energy needed for excitations across the gap [51]. In contrast to one-dimensional systems, in higher-dimensional materials not all electronic bands might be affected by the CDW formation, leading to a partial gap opening only. Prominent examples of materials showing the development of CDWs are the quasi-1D blue bronze $K_{0.3}MoO_3$ [21,52,53], quasi-1D $(TaSe_4)_2I$ [54,55], and the square-net rare-earth ditellurides ($LnTe_2$) [1,24–30]. Also for *Ln*SbTe with *Ln*= La, Ce, Gd, Ho it was suggested that the MIR absorption peaks in the optical conductivity spectra are signatures of CDW gaps [17,33].

It is, however, important to note that for stoichiometric GdSbTe the development of CDWs is not expected, since no direct experimental evidence for lattice distortions related to CDWs has been reported according to our knowledge [35]. Besides, GdSbTe is isostructural to the prototype nodal-line semimetal ZrSiS and to LaSbTe. The three materials show strong similarities in their electronic band structure, even when SOC is taken into account [3,10,13,56]. Accordingly, similarities in their optical responses are expected. For comparison, the optical conductivity spectrum of ZrSiS at 5 K is depicted in Fig. 3(b). It has a characteristic U shape related to excitations of the topologically nontrivial electronic bands followed by a peak at high energy due to transitions between parallel bands [44]. An MIR absorption band as reported for GdSbTe [33] is, however, not observed.

In contrast, for nonstoichiometric compounds $GdSb_xTe_{2-x-\delta}$ with Sb content x smaller than 0.85 the presence of CDWs has been evidenced by x-ray diffraction and transmission electron microscopy (TEM) [16,35]. The optical conductivity spectra of $GdSb_{0.56}Te_{1.35}$ and $GdSb_{0.45}Te_{1.50}$ are consistent with the presence of CDWs: As compared to ZrSiS, the optical conductivity is drastically reduced [see Fig. 3(b)]. Furthermore, both materials exhibit a small low-frequency conductivity and a pronounced NIR absorption band in the optical spectrum, which could be, at least partially, attributed to excitations across the CDW gap. It needs to be noted that the slight temperature dependence of the σ_1 spectrum of $GdSb_{0.45}Te_{1.50}$ for E∥a [see Fig. 5(b)] is not consistent with the general CDW picture, since a shift of spectral weight to higher frequencies with decreasing temperature would be expected (though other exceptions have been reported in the literature [57]). A possible reason is that the absorption feature may also contain contributions from electronic bands close to E_F, which are not affected by the CDW formation, as has been pointed out previously [16].

The interrelation between stoichiometry and structural, electronic, and magnetic properties has been discussed in detail in Refs. [16,35]. For $x < 0.85$ the crystal symmetry is orthorhombic (space group *Pmmn*) with slight differences in the in-plane lattice parameters a and b. Five representative compounds were characterized for possible CDW related superstructure modulations by TEM: The results revealed superstructure reflections for $GdSb_{0.06}Te_{1.82}$, $GdSb_{0.21}Te_{1.70}$, and $GdSb_{0.45}Te_{1.53}$, but not for $GdSb_{0.79}Te_{1.20}$ and $GdSb_{0.85}Te_{1.82}$. Concomitant with the presence of a CDW for reduced Sb content are energy gaps in the electronic band structure close to E_F and a shift of the Fermi level to higher energies. ARPES studies combined with DFT calculations on $GdSb_{0.46}Te_{1.48}$ revealed the presence of a CDW gap in several bands, while the nonsymmorphic symmetry preserves the Dirac crossings at high symmetry points and the NL along the X-U direction [16].

Accordingly, in the case of the two compositions studied here, we expect that the CDW formation related to the complex interplay between Fermi surface nesting and the momentum and orbital-dependent electron-phonon coupling [35] is more clearly developed for $GdSb_{0.45}Te_{1.50}$ as compared to $GdSb_{0.56}Te_{1.35}$. This is consistent with our findings: For $GdSb_{0.45}Te_{1.50}$ the Drude contribution related to itinerant charge carriers is much more suppressed and the in-plane optical response is anisotropic, as compared to $GdSb_{0.56}Te_{1.35}$ [Fig. 5(b)]. The size of the CDW gap is enhanced from ∼5400 cm^{-1} (∼0.67 eV) for $GdSb_{0.56}Te_{1.35}$ to the values ∼7100 cm^{-1} (∼0.88 eV) and ∼8700 cm^{-1} (∼1.08 eV) for $GdSb_{0.45}Te_{1.50}$. According to our optical data, the band structure is fully gapped at E_F in the case of $GdSb_{0.45}Te_{1.50}$.

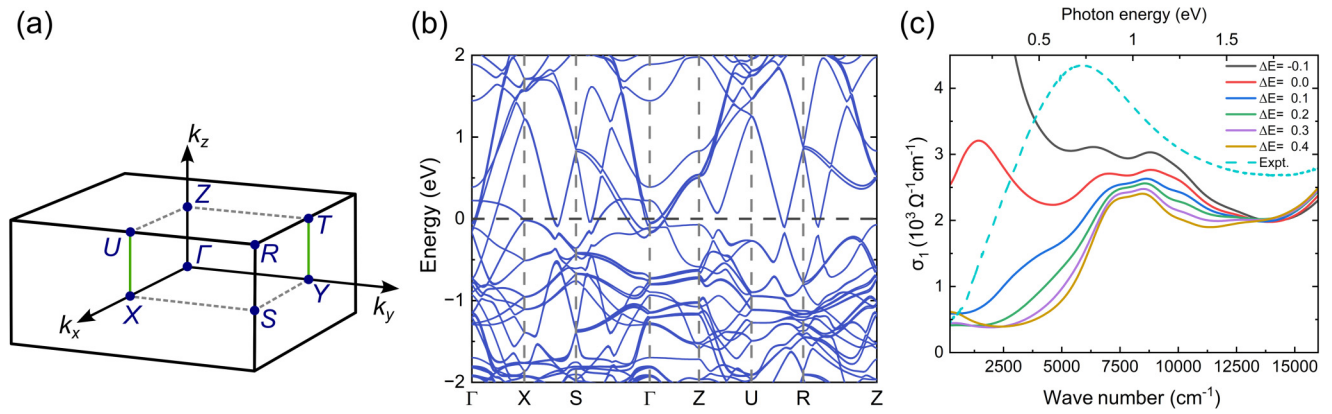

FIG. 7. (a) Schematic representation of the bulk Brillouin zone with the high-symmetry points. Green line indicates the NL along X-U and Y-T. (b) Electronic band structure with spin-orbit coupling (SOC) and Hubbard $U = 6$ eV for the AFM-A configuration. (c) Optical conductivity (σ_{xx}) spectra of the AFM-A configuration at different Fermi energy shifts (ΔE), compared with the optical conductivity spectra of $GdSb_{0.56}Ge_{1.35}$. Here, $\Delta E = E - E_F$ denotes the energy difference relative to the calculated Fermi level of GdSbTe.

Finally, we would like to comment on the observed difference in the polarization dependence of the optical responses between $GdSb_{0.56}Te_{1.35}$ (no polarization dependence) and $GdSb_{0.45}Te_{1.50}$ (polarization dependence). According to previous studies, the system often features multiple CDW domains, which can obscure anisotropic optical responses. In single crystals of $GdSb_xTe_{2-x-\delta}$, CDW domains can reach widths of up to ∼100 μm [16,34], depending on the Sb content, x. For $x \gtrsim 0.2$, the domain size tends to increase as the Sb content decreases, in accordance with an increasing difference between the two in-plane lattice constants: a and b. Therefore, larger CDW domains are expected for $GdSb_{0.45}Te_{1.50}$ than for $GdSb_{0.56}Te_{1.35}$. Given our measurement geometry, with a beam spot size of ∼200 μm), it is not guaranteed that the measurement was conducted on a single CDW domain. In the case of $GdSb_{0.56}Te_{1.35}$, where the domain width is ∼10 μm, the measured response effectively averages over multiple domains with perpendicular CDW wave vectors, leading to a cancellation of polarization dependence. While in case of $GdSb_{0.45}Te_{1.50}$, the optical measurements can access a larger area of one type of CDW domain than the other, thereby preserving polarization-dependent features in the optical response.

D. Theoretical optical conductivity

Calculations of interband optical conductivity based on electronic band structures provide valuable theoretical insights. Although achieving a quantitative description of optical conductivity remains challenging in semimetallic systems, theoretical results can still offer qualitative agreement with experimental observations [58–60]. Here, we consider several possible magnetic configurations of GdSbTe, as illustrated in Fig. S1 in the Supplemental Material [45], including AFM-A, antiferromagnetic coupling along the in-plane direction (AFM-I), and antiferromagnetic coupling along the out-of-plane direction (AFM-Z). According to previous studies, the AFM-A configuration is most consistent with experimental magnetic susceptibility measurements [14,15]. Consequently, we focus on this configuration and calculate the corresponding electronic band structure, as shown in Fig. 7(b). The magnetic moment of the Gd atom was calculated to be 7.0 μ_B per atom, in good agreement with the reported values [15]. The calculated electronic band structure confirms that the AFM compound GdSbTe is semimetallic. As depicted in Figs. S2 and S3 in the Supplemental Material [45], variations in the magnetic configuration have no significant effect on the band structure. Using the d and f orbitals of Gd atoms and the s and p orbitals of Sb and Te atoms as the basis set, we constructed the WANNIER Hamiltonian from first-principles results via the WANNIER90 code [42]. This WANNIER Hamiltonian successfully reproduces the first-principles band structure, as plotted in Fig. S5 in the Supplemental Material [45]. Using the WANNIERBERRI code, the interband optical conductivity $\sigma(\omega)$ is evaluated based on the Kubo-Greenwood formula [42,43],

$$\sigma_{\alpha\beta}(\omega) = \frac{ie^2\hbar}{N_k\Omega_c}\sum_{\mathbf{k},n,m}\frac{f_{mk}(T) - f_{nk}(T)}{\varepsilon_{mk} - \varepsilon_{nk}} \times \frac{\langle\psi_{nk}|v_\alpha|\psi_{mk}\rangle\langle\psi_{mk}|v_\beta|\psi_{nk}\rangle}{\varepsilon_{mk} - \varepsilon_{nk} - (\hbar\omega + i\eta)}, \quad (2)$$

where α, β denote Cartesian directions, Ω_c is the cell volume, N_k is the number of k points used for sampling the Brillouin zone, and $f_{nk}(T)$ is the Fermi-Dirac distribution function at temperature T, which is set to 0 K in our calculations. $\hbar\omega$ is the optical frequency, and η is a smearing parameter set to 0.1 eV.

Since the calculations are based on a stoichiometric structure, the Fermi level of the actual compound $GdSb_{0.56}Te_{1.35}$, which is affected by doping, is expected to shift to a higher energy region. Therefore, we calculated the interband optical conductivity for several shifted Fermi levels, as shown in Fig. 7(c) with solid lines. For the calculated Fermi level corresponding to the undoped system, the interband conductivity shows a large value in the low-frequency region, indicating abundant low-energy interband transitions. As the Fermi level is increased, the low-frequency interband conductivity decreases significantly, showing better agreement with the experimental results. In the higher-frequency region, the calculated conductivity exhibits an almost flat behavior, which is in agreement with the experimental features. Additionally, the optical conductivity was calculated for various magnetic

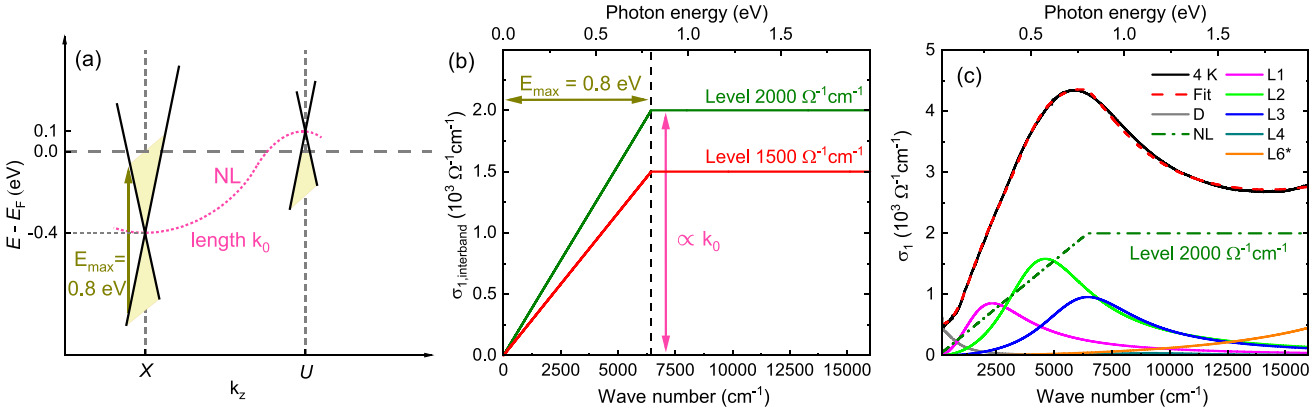

FIG. 8. (a) Illustration of the Dirac nodal line (NL) with length k_0 in $GdSb_{0.56}Te_{1.35}$ along the X-U direction of the Brillouin zone. The maximum shift of the NL away from the Fermi energy E_F is given by $E_{max}/2$. (b) Interband optical conductivity $\sigma_{1,interband}$ of a dispersive NL with the levels 1500 and 2000 $\Omega^{-1}cm^{-1}$, which correspond to the length k_0 of the NL according to Eq. (3). (c) Optical conductivity σ_1 of $GdSb_{0.56}Te_{1.35}$ at 4 K, together with the total NL-Drude-Lorentz fit and the various fit contributions, including the nodal-line term with the level 2000 $\Omega^{-1}cm^{-1}$.

configurations, as shown in Figs. S2 and S3 in the Supplemental Material [45]. These results indicate that the optical response of GdSbTe is insensitive to the magnetic ordering.

E. Signatures of Dirac fermion excitations in $GdSb_{0.56}Te_{1.35}$?

Similar to the closely related compound ZrSiS, GdSbTe is considered as a nodal-line semimetal, where Dirac fermion excitations are expected to contribute to the optical response. Interband transitions in Dirac cones will lead to a characteristic shape of the optical conductivity spectrum, following a distinct power law according to $\sigma_1(\omega) \propto \omega^{d-2}$, depending on the dimensionality d of the Dirac bands [61–64]. Hence, for three-dimensional (3D) Dirac fermions, a linear-in-frequency behavior, $\sigma_1(\omega) \propto \omega$, is expected. As the Dirac fermions in nodal-line semimetals are effectively 2D, a frequency-independent (flat) optical conductivity is expected, whose level can serve as an estimate for the length k_0 of the NL in reciprocal space according to

$$\sigma_{1,\mathrm{flat}} = \frac{e^2 k_0}{16\hbar} \quad , \tag{3}$$

where a circular NL oriented perpendicular to the electric field of the incoming electromagnetic radiation is considered [65–67].

For a dispersive NL, which is the case in GdSbTe, the low-energy optical conductivity due to interband transitions resembles that of isolated 3D Dirac cones, following a linear-in-frequency behavior $\sigma_1(\omega) \propto \omega$ [63]. Above the energy E_{max}, which is twice the maximum shift of the NL away from the Fermi energy, the optical conductivity becomes flat and resembles that of a dispersionless NL [63]. The level of the frequency-independent part of $\sigma_1(\omega)$ again can serve as a rough estimate of the length k_0 of the NL according to Eq. (3).

The existence of a dispersive NL in nonstoichimetric $GdSb_{0.46}Te_{1.48}$ is confirmed by the studies of Lei *et al.* [16], a combination of theoretical calculations and angle-resolved photoemission spectroscopy measurements. Moreover, the nonsymmorphic Dirac points at X and U are considered as stable in both the antiferromagnetic and paramagnetic phases [14,15]. These linear band touching points are symmetry protected from SOC gapping. For the nonstoichimetric compound $GdSb_{0.46}Te_{1.48}$ the CDW preserves the nonsymmorphic symmetry, and therefore the NL along X-U is barely affected by the CDW distortions of the crystal lattice [16]. Thus, we may apply the above formalism, in order to estimate the nodal line length in nonstoichiometric GdSbTe based on our optical data.

As sketched in Fig. 8(a), the Dirac crossing points at the X and U points of the Brillouin zone are connected by a dispersive NL crossing the Fermi level E_F. For GdSbTe the maximum shift of the NL away from E_F occurs at the U point and amounts to 0.4 eV. For $GdSb_{0.46}Te_{1.48}$, E_F is shifted up and is located at the Dirac node at U [16]. In the case of $GdSb_{0.56}Te_{1.35}$ with slightly larger Sb content we assume a Fermi level ~0.1 eV below this Dirac node, resulting in the value $E_{max} = 0.8$ eV. In Fig. 8(b) we simulate the contribution to the optical conductivity resulting from interband excitations of the dispersive NL in $GdSb_{0.56}Te_{1.35}$ with $E_{max} = 0.8$ eV and two different lengths k_0 corresponding to two different $\sigma_{1,flat}$ levels 1500 and 2000 $\Omega^{-1}cm^{-1}$ [see Eq. (3)].

We incorporated the contributions of interband transitions of the dispersive NL in the Drude-Lorentz fit model, in order to describe the total optical conductivity σ_1 of $GdSb_{0.56}Te_{1.35}$ at 4 K. A good fit of the experimental data can be achieved with a maximum $\sigma_{1,flat}$ level of 1800–2000 $\Omega^{-1}cm^{-1}$. For higher levels, the total fit is significantly worse, as shown in Fig. S9 in the Supplemental Material [45]. This result sets a maximum length $k_{0,max} = 1.2$–1.3 Å^{-1} of the dispersive NL. To validate this result further, we compared $k_{0,max}$ with the value derived from band structure calculations based on the lattice parameters of our material. The nodal line is expected to extend along the X-U direction, forming an approximately straight line parallel to the [001] direction. From the corresponding Brillouin zone dimensions, we can estimate the nodal-line length to be $k_0 \sim 0.69$ Å^{-1}. Although this value is smaller than the $k_{0,max}$ value determined experimentally, it lies within the same order of magnitude, thus confirming the plausibility of our findings. It is furthermore interesting to note, that studies by Schilling *et al.* estimated a nodal-line

length of $k_0 = 4.3\,\text{Å}^{-1}$ for ZrSiS [68], whereas Shao *et al.* obtained $k_0 = 0.2\,\text{Å}^{-1}$ for the dispersive NL in $NbAs_2$ [63]. Compared to these findings, our estimated maximum NL length is intermediate and of the same order of magnitude.

Finally, we note that a linear-in-frequency increase followed by a rather flat behavior is also present and even more clearly seen in the optical conductivity spectrum of $GdSb_{0.45}Te_{1.50}$, especially along the CDW direction [see Fig. 5(b)]. From the level $\sigma_{1,\text{flat}} \approx 2000\,\Omega^{-1}\text{cm}^{-1}$ we estimate a maximum length $k_{0,\text{max}} \approx 1.3\,\text{Å}^{-1}$ of the dispersive NL according to Eq. (3), which is close to the value for $GdSb_{0.56}Te_{1.35}$. This result is also in agreement with the findings in Ref. [16] for $GdSb_{0.46}Te_{1.48}$ (i.e., with a very similar composition), which evidence the presence of a dispersive NL close to E_F in nonstoichiometric compounds, while other trivial electronic bands being removed as a result of the CDW lattice distortion. In analogy to $GdSb_{0.46}Te_{1.48}$, we expect the NL in $GdSb_{0.45}Te_{1.50}$ to cross E_F at the U point of the Brillouin zone. In this case the onset of the linear-in-frequency behavior of σ_1 would occur at zero frequency. According to our experimental results the onset occurs above approximately $2500\,\text{cm}^{-1}$ (0.31 eV), which means that the electronic band structure is fully gapped at E_F, including the NL states, due to the CDW distortions.

IV. CONCLUSION

In conclusion, we studied the in-plane optical conductivity of the Dirac semimetals $GdSb_{0.56}Te_{1.35}$ and $GdSb_{0.45}Te_{1.50}$ as a function of temperature and polarization direction of the radiation. According to our results, already small differences in stoichiometry have a big impact on the optical response: While $GdSb_{0.56}Te_{1.35}$ shows no in-plane anisotropy and a weak metallic character, in $GdSb_{0.45}Te_{1.50}$ the optical response is polarization dependent and the metallic character is strongly reduced. For both materials the optical conductivity spectrum contains a NIR absorption band, which we interpret in terms of excitations across a CDW gap. For $GdSb_{0.56}Te_{1.35}$ the optical response exhibits no significant temperature dependence and no signatures associated with magnetic ordering are detected, indicating a negligible coupling between magnetic and charge degrees of freedom. Our DFT calculations of the interband optical conductivity qualitatively capture the main experimental features and demonstrate that the optical response of GdSbTe is robust against magnetic ordering. We also analyzed the optical conductivity spectra in terms of excitations of Dirac fermion excitations and estimate the maximum length of the dispersive nodal line. Our findings call for further investigations on the interplay of charge-density-wave distortion, magnetism, and band topology in $LnSb_xTe_{2-x-\delta}$ materials.

ACKNOWLEDGMENTS

S.R. and R.B. acknowledge technical support by Jihaan Ebad-Allah, Beate Spörhase, and Susanne Denzer. C.A.K. acknowledges financial support by the Deutsche Forschungsgemeinschaft (DFG), Germany, through Grants No. KU 1432/13-2 and No. TRR 360 – 492547816 (subproject A1). Work at Princeton was supported by an NSF CAREER grant (DMR-2144295) to L.M.S. Additional support was provided by the Air Force office of Scientific Research under Award No. FA9550-23-1-0635. R.S. acknowledges the financial support provided by the Ministry of Science and Technology in Taiwan under Projects No. NSTC-114-2124-M-001-009 and NSTC-113-2112M001045-MY3, as well as support from Academia Sinica for the budget of AS-iMATE11514. M.G.V. thanks support to PID2022-142008NB-I00 funded by MICIU/AEI/10.13039/501100011033 and FEDER, UE, and to Diputación Foral de Gipuzkoa Programa Mujeres y Ciencia. Work at Sherbrooke was supported by the Canada Excellence Research Chairs Program for Topological Quantum Matter to M.G.V.

DATA AVAILABILITY

The data that support the findings of this article are openly available [69].

[1] S. Klemenz, A. K. Hay, S. M. L. Teicher, A. Topp, J. Cano, and L. M. Schoop, The role of delocalized chemical bonding in square-net-based topological semimetals, J. Am. Chem. Soc. **142**, 6350 (2020).

[2] M. Neupane, I. Belopolski, M. M. Hosen, D. S. Sanchez, R. Sankar, M. Szlawska, S.-Y. Xu, K. Dimitri, N. Dhakal, P. Maldonado, P. M. Oppeneer, D. Kaczorowski, F. Chou, M. Z. Hasan, and T. Durakiewicz, Observation of topological nodal fermion semimetal phase in ZrSiS, Phys. Rev. B **93**, 201104(R) (2016).

[3] L. M. Schoop, M. N. Ali, C. Strasser, A. Topp, A. Varykhalov, D. Marchenko, V. Duppel, S. S. P. Parkin, B. V. Lotsch, and C. R. Ast, Dirac cone protected by non-symmorphic symmetry and three-dimensional Dirac line node in ZrSiS, Nat. Commun. **7**, 11696 (2016).

[4] A. Topp, J. M. Lippmann, A. Varykhalov, V. Duppel, B. V. Lotsch, C. R. Ast, and L. M. Schoop, Non-symmorphic band degeneracy at the Fermi level in ZrSiTe, New J. Phys. **18**, 125014 (2016).

[5] Y.-Y. Lv, B.-B. Zhang, X. Li, S.-H. Yao, Y. B. Chen, J. Zhou, S.-T. Zhang, M.-H. Lu, and Y.-F. Chen, Extremely large and significantly anisotropic magnetoresistance in ZrSiS single crystals, Appl. Phys. Lett. **108**, 244101 (2016).

[6] R. Sankar, G. Peramaiyan, I. P. Muthuselvam, C. J. Butler, K. Dimitri, M. Neupane, G. N. Rao, M.-T. Lin, and F. C. Chou, Crystal growth of Dirac semimetal ZrSiS with high magnetoresistance and mobility, Sci. Rep. **7**, 40603 (2017).

[7] J. Hu, Z. Tang, J. Liu, Y. Zhu, J. Wei, and Z. Mao, Nearly massless Dirac fermions and strong Zeeman splitting in the nodal-line semimetal ZrSiS probed by de Haas–van Alphen quantum oscillations, Phys. Rev. B **96**, 045127 (2017).

[8] C. Wang and T. Hughbanks, Main group element size and substitution effects on the structural dimensionality of zirconium tellurides of the ZrSiS type, Inorg. Chem. **34**, 5524 (1995).

[9] S. Klemenz, S. Lei, and L. M. Schoop, Topological semimetals in square-net materials, Annu. Rev. Mater. Res. **49**, 185 (2019).

[10] J. Ebad-Allah, J. Fernández Afonso, M. Krottenmüller, J. Hu, Y. L. Zhu, Z. Q. Mao, J. Kunes, and C. A. Kuntscher, Chemical pressure effect on the optical conductivity of the nodal-line semimetals ZrSiY (Y=S,Se,Te) and ZrGeY (Y=S,Te), Phys. Rev. B **99**, 125154 (2019).

[11] L. M. Schoop, A. Topp, J. Lippmann, F. Orlandi, L. Müchler, M. G. Vergniory, Y. Sun, A. W. Rost, V. Duppel, M. Krivenkov, S. Sheoran, P. Manuel, A. Varykhalov, B. Yan, R. K. Kremer, C. R. Ast, and B. V. Lotsch, Tunable Weyl and Dirac states in the nonsymmorphic compound CeSbTe, Sci. Adv. **4**, eaar2317 (2018).

[12] S. Regmi, G. Dhakal, F. C. Kabeer, N. Harrison, F. Kabir, A. P. Sakhya, K. Gofryk, D. Kaczorowski, P. M. Oppeneer, and M. Neupane, Observation of multiple nodal-lines in SmSbTe, Phys. Rev. Mater. **6**, L031201 (2022).

[13] Y.T. Qian, Z.Y. Tan, T. Zhang, J.C. Gao, Z.J. Wang, Z. Fang, C. Fang, and H.M. Weng, Layer construction of topological crystalline insulator LaSbTe, Sci. China Phys. Mech. Astron. **63**, 107011 (2020).

[14] M. M. Hosen, G. Dhakal, K. Dimitri, P. Maldonado, A. Aperis, F. Kabir, C. Sims, P. Riseborough, P. M. Oppeneer, D. Kaczorowski, T. Durakiewicz, and M. Neupane, Discovery of topological nodal-line fermionic phase in a magnetic material GdSbTe, Sci. Rep. **8**, 13283 (2018).

[15] R. Sankar, I. P. Muthuselvam, K. R. Babu, G. S. Murugan, K. Rajagopal, R. Kumar, T.-C. Wu, C.-Y. Wen, W.-L. Lee, G.-Y. Guo, and F.-C. Chou, Crystal growth and magnetic properties of topological nodal-line semimetal GdSbTe with antiferromagnetic spin ordering, Inorg. Chem. **58**, 11730 (2019).

[16] S. Lei, S. M. L. Teicher, A. Topp, K. Cai, J. Lin, G. Cheng, T. H. Salters, F. Rodolakis, J. L. McChesney, S. Lapidus, N. Yao, M. Krivenkov, D. Marchenko, A. Varykhalov, C. R. Ast, R. Car, J. Cano, M. G. Vergniory, N. P. Ong, and L. M. Schoop, Band engineering of Dirac semimetals using charge density waves, Adv. Mater. **33**, 2101591 (2021).

[17] J. L. Liu, R. Liu, M. Yang, L. Y. Cao, B. X. Gao, L. Wang, A. F. Fang, Y. G. Shi, Z. P. Yin, and R. Y. Chen, Revealing a charge-density-wave gap in the predicted weak topological insulator HoSbTe, Phys. Rev. B **105**, 075111 (2022).

[18] R. Singha, A. Pariari, B. Satpati, and P. Mandal, Magnetotransport properties and evidence of a topological insulating state in LaSbTe, Phys. Rev. B **96**, 245138 (2017).

[19] The dc conductivity of GdSbTe amounts to 270–333 $\Omega^{-1}\text{cm}^{-1}$ at room temperature (RT) and decreases with decreasing temperature [15]. In comparison, ZrSiS [6] and LaSbTe [18] have a RT conductivity of $5 \times 10^4\Omega^{-1}\text{cm}^{-1}$ and $1.2 \times 10^4\Omega^{-1}\text{cm}^{-1}$, respectively, with increasing values during cooling.

[20] R. E. Peierls, *Quantum Theory of Solids* (Clarendon, Oxford, 1955).

[21] G. Grüner, *Density Waves in Solids* (Addison Wesley, 1994), pp. 55–70.

[22] P. Chen, W. Pai, Y.-H. Chan, A. Takayama, C.-Z. Xu, A. Karn, S. Hasegawa, M. Y. Chou, S.-K. Mo, A.-V. Fedorov, and T.-C. Chiang, Emergence of charge density waves and a pseudogap in single-layer $TiTe_2$, Nat. Commun. **8**, 516 (2017).

[23] D. Le Bolloc'h, A. A. Sinchenko, V. L. R. Jacques, L. Ortega, J. E. Lorenzo, G. A. Chahine, P. Lejay, and P. Monceau, Effect of dimensionality on sliding charge density waves: The quasi-two-dimensional $TbTe_3$ system probed by coherent x-ray diffraction, Phys. Rev. B **93**, 165124 (2016).

[24] A. Kikuchi, Electronic structure of lanthan ditellurides, J. Phys. Soc. Jpn. **67**, 1308 (1998).

[25] M. H. Jung, T. Ekino, Y. S. Kwon, and T. Takabatake, Tunneling spectroscopy of RTe_2(R = La, Ce) and possible coexistence between charge-density waves and magnetic order, Phys. Rev. B **63**, 035101 (2000).

[26] J. H. Shim, J.-S. Kang, and B. I. Min, Electronic structures of RTe_2 (R = La, Ce): A clue to the pressure-induced superconductivity in $CeTe_{1.82}$, Phys. Rev. Lett. **93**, 156406 (2004).

[27] J.-S. Kang, C. G. Olson, Y. S. Kwon, J. H. Shim, and B. I. Min, Charge-density wave gap and Ce $4f$ states in $CeTe_2$ observed by photoemission spectroscopy, Phys. Rev. B **74**, 085115 (2006).

[28] D. R. Garcia, G.-H. Gweon, S. Y. Zhou, J. Graf, C. M. Jozwiak, M. H. Jung, Y. S. Kwon, and A. Lanzara, Revealing charge density wave formation in the $LaTe_2$ system by angle resolved photoemission spectroscopy, Phys. Rev. Lett. **98**, 166403 (2007).

[29] J.-S. Kang, D. H. Kim, H. J. Lee, J. Hwang, H.-K. Lee, H.-D. Kim, B. H. Min, K. E. Lee, Y. S. Kwon, J. W. Kim, K. Kim, B. H. Kim, and B. I. Min, Fermi surface reconstruction in $CeTe_2$ induced by charge density waves investigated via angle resolved photoemission, Phys. Rev. B **85**, 085104 (2012).

[30] E. Lee, D. H. Kim, J. D. Denlinger, J. Kim, K. Kim, B. I. Min, B. H. Min, Y. S. Kwon, and J.-S. Kang, Angle-resolved and resonant photoemission spectroscopy study of the Fermi surface reconstruction in the charge density wave systems $CeTe_2$ and $PrTe_2$, Phys. Rev. B **91**, 125137 (2015).

[31] P. Li, B.J. Lv, Y. Fang, W. Guo, Z.Z. Wu, Y. Wu, D.W. Shen, Y.F. Nie, L. Petaccia, C. Cao, Z.-A. Xu, and Liu Y., Charge density wave and weak Kondo effect in a Dirac semimetal CeSbTe, Sci. China Phys. Mech. Astron. **64**, 237412 (2021).

[32] E. DiMasi, B. Foran, M. C. Aronson, and S. Lee, Stability of charge-density waves under continuous variation of band filling in $LaTe_{2-x}Sb_x$ ($0 \leqslant x \leqslant 1$), Phys. Rev. B **54**, 13587 (1996).

[33] L. Y. Cao, M. Yang, L. Wang, Y. Li, B. X. Gao, L. Wang, J. L. Liu, A. F. Fang, Y. G. Shi, and R. Y. Chen, Optical study of the topological materials LnSbTe(Ln = La, Ce, Sm, Gd), Phys. Rev. B **106**, 245145 (2022).

[34] S. Lei, A. Saltzman, and L. M. Schoop, Complex magnetic phases enriched by charge density waves in the topological semimetals $GdSb_xTe_{2-x-\delta}$, Phys. Rev. B **103**, 134418 (2021).

[35] S. Lei, V. Duppel, J. Lippmann, B. Nuss, B. V. Lotsch, and L. M. Schoop, Charge density waves and magnetism in topological semimetal candidates $GdSb_xTe_{2-x-\delta}$, Adv. Quantum Technol. **2**, 1900045 (2019).

[36] T. H. Salters, J. Colagiuri, A. K. Liston, J. Leeman, T. Berry, and L. M. Schoop, Synthesis and stability phase diagram of topological semimetal family $LnSb_xTe_{2-x-\delta}$, Chem. Mater. **36**, 11873 (2024).

[37] D. B. Tanner, Use of x-ray scattering functions in Kramers-Kronig analysis of reflectance, Phys. Rev. B **91**, 035123 (2015).

[38] A. B. Kuzmenko, Kramers–Kronig constrained variational analysis of optical spectra, Rev. Sci. Instrum. **76**, 083108 (2005).

[39] G. Kresse and J. Hafner, *Ab initio* molecular dynamics for liquid metals, Phys. Rev. B **47**, 558 (1993).

[40] G. Kresse and J. Furthmüller, Efficient iterative schemes for *ab initio* total-energy calculations using a plane-wave basis set, Phys. Rev. B **54**, 11169 (1996).

[41] J. P. Perdew, K. Burke, and M. Ernzerhof, Generalized gradient approximation made simple, Phys. Rev. Lett. **77**, 3865 (1996).

[42] G. Pizzi, V. Vitale, R. Arita, S. Blügel, F. Freimuth, G. Géranton, M. Gibertini, D. Gresch, C. Johnson, T. Koretsune, J. Ibañez-Azpiroz, H. Lee, J.-M. Lihm, D. Marchand, A. Marrazzo, Y. Mokrousov, J. Mustafa, Y. Nohara, Y. Nomura, L. Paulatto, *et al.*, WANNIER90 as a community code: New features and applications, J. Phys.: Condens. Matter **32**, 165902 (2020).

[43] S. S. Tsirkin, High performance WANNIER interpolation of Berry curvature and related quantities with WANNIERBERRI code, npj Comput. Mater. **7**, 33 (2021).

[44] J. Ebad-Allah, S. Rojewski, M. Vöst, G. Eickerling, W. Scherer, E. Uykur, R. Sankar, L. Varrassi, C. Franchini, K.-H. Ahn, J. Kuneš, and C. A. Kuntscher, Pressure-induced excitations in the out-of-plane optical response of the nodal-line semimetal ZrSiS, Phys. Rev. Lett. **127**, 076402 (2021).

[45] See Supplemental Material at http://link.aps.org/supplemental/10.1103/nygm-n4fv for additional theoretical and experimental results.

[46] M. Dressel and G. Grüner, *Electrodynamics of Solids - Optical Properties of Electrons in Matter* (Cambridge University Press, Cambridge, UK, 2002).

[47] A. Perucchi, L. Degiorgi, and H. Berger, Infrared signature of the charge-density-wave gap in $ZrTe_3$, Eur. Phys. J. B **48**, 489 (2005).

[48] M. M. May, C. Brabetz, C. Janowitz, and R. Manzke, CDW phase of $1T$-$TiSe_2$: The influence of conduction band population, Phys. Rev. Lett. **107**, 176405 (2011).

[49] A. Zong, *Emergent States in Photoinduced Charge-Density-Wave Transitions* (Springer, 2021).

[50] L. Degiorgi, F.B.B. Anders, and G. Grüner, Charge excitations in heavy electron metals, Eur. Phys. J. B **19**, 167 (2001).

[51] S. Das, G. L. Prajapati, R. Rana, and D. S. Rana, Probing low energy dynamics in charge-ordered $NdNiO_3$ by terahertz time domain spectroscopy, Vacuum **151**, 73 (2018).

[52] B. P. Gorshunov, A. A. Volkov, G. V. Kozlov, L. Degiorgi, A. Blank, T. Csiba, M. Dressel, Y. Kim, A. Schwartz, and G. Grüner, Charge-density-wave paraconductivity in $K_{0.3}MoO_3$, Phys. Rev. Lett. **73**, 308 (1994).

[53] L. P. Gor'kov and G. Grüner, *Charge Density Waves in Solids* (Elsevier B.V., 1989), Vol. 25.

[54] R. J. Cava, P. Littlewood, R. M. Fleming, R. G. Dunn, and E. A. Rietman, Low-frequency dielectric response of the charge-density wave in $(TaSe_4)_2I$, Phys. Rev. B **33**, 2439 (1986).

[55] J. Gooth, B. Bradlyn, S. Honnali, C. Schindler, N. Kumar, J. Noky, Y. Qi, C. Shekhar, Y. Sun, Z. Wang, B. A. Bernevig, and C. Felser, Axionic charge-density wave in the Weyl semimetal $(TaSe_4)_2I$, Nature (London) **575**, 315 (2019).

[56] Y. Wang, Y. Qian, M. Yang, H. Chen, C. Li, Z. Tan, Y. Cai, W. Zhao, S. Gao, Y. Feng, S. Kumar, E. F. Schwier, L. Zhao, H. Weng, Y. Shi, G. Wang, Y. Song, Y. Huang, K. Shimada, Z. Xu, *et al.*, Spectroscopic evidence for the realization of a genuine topological nodal-line semimetal in LaSbTe, Phys. Rev. B **103**, 125131 (2021).

[57] K. E. Lee, C. I. Lee, H. J. Oh, M. A. Jung, B. H. Min, H. J. Im, T. Iizuka, Y. S. Lee, S. Kimura, and Y. S. Kwon, Optical properties of the charge-density-wave compound $CeTe_2$, Phys. Rev. B **78**, 134408 (2008).

[58] D. Chaudhuri, B. Cheng, A. Yaresko, Q. D. Gibson, R. J. Cava, and N. P. Armitage, Optical investigation of the strong spin-orbit-coupled magnetic semimetal $YbMnBi_2$, Phys. Rev. B **96**, 075151 (2017).

[59] Shin-ichi Kimura, H. Yokoyama, H. Watanabe, J. Sichelschmidt, V. Süß, M. Schmidt, and C. Felser, Optical signature of Weyl electronic structures in tantalum pnictides Ta Pn (Pn = P, As), Phys. Rev. B **96**, 075119 (2017).

[60] D. Neubauer, A. Yaresko, W. Li, A. Löhle, R. Hübner, M. B. Schilling, C. Shekhar, C. Felser, M. Dressel, and A. V. Pronin, Optical conductivity of the Weyl semimetal NbP, Phys. Rev. B **98**, 195203 (2018).

[61] P. Hosur, S. A. Parameswaran, and A. Vishwanath, Charge transport in Weyl semimetals, Phys. Rev. Lett. **108**, 046602 (2012).

[62] A. Bacsi and A. Virosztek, Low-frequency optical conductivity in graphene and in other scale-invariant two-band systems, Phys. Rev. B **87**, 125425 (2013).

[63] Y. M. Shao, Z. Y. Sun, Y. Wang, C. C. Xu, R. Sankar, A. J. Breindel, C. Cao, M. M. Fogler, F. C. Chou, Z. Q. Li, T. Timusk, M. B. Maple, and D. N. Basov, Optical signatures of Dirac nodal lines in $NbAs_2$, Proc. Natl. Acad. Sci. USA **116**, 1168 (2019).

[64] N. P. Armitage, E. J. Mele, and A. Vishwanath, Weyl and Dirac semimetals in three-dimensional solids, Rev. Mod. Phys. **90**, 015001 (2018).

[65] J. P. Carbotte, Optical response of a line node semimetal, J. Phys.: Condens. Matter **29**, 045301 (2017).

[66] S. P. Mukherjee and J. P. Carbotte, Transport and optics at the node in a nodal loop semimetal, Phys. Rev. B **95**, 214203 (2017).

[67] S. Ahn, E. J. Mele, and H. Min, Electrodynamics on Fermi cyclides in nodal line semimetals, Phys. Rev. Lett. **119**, 147402 (2017).

[68] M. B. Schilling, L. M. Schoop, B. V. Lotsch, M. Dressel, and A. V. Pronin, Flat optical conductivity in ZrSiS due to two-dimensional Dirac bands, Phys. Rev. Lett. **119**, 187401 (2017).

[69] S. Rojewski, R. Borkenhagen, R. Li, D. G. Ovalle, S. S. Tsirkin, H. Kumar, K. Raju, R. Sankar, S. Lei, L. M. Schoop, M. G. Vergniory, and C. A. Kuntscher, Optical response of the Dirac semimetals $GdSb_{0.56}Te_{1.35}$ and $GdSb_{0.45}Te_{1.50}$: Influence of charge-density-wave distortion and magnetic order [Data set], Zenodo (2026), 10.5281/zenodo.19235004.